Ultraporous Electron-Depleted ZnO Nanoparticle Networks for Highly Sensitive Portable Visible-Blind UV-Photodetectors

Noushin Nasiri[1], Renheng Bo[1], Fan Wang[2], Lan Fu[2], Antonio Tricoli[1] *

[1]Nanotechnology Research Laboratory, Research School of Engineering, Australian National University, Canberra 2601, Australia
[2]Department of Electronic Materials Engineering, College of Physical and Mathematical Sciences, Australian National University, Canberra 2601, Australia

Keywords: UV photodetector, ZnO nanoparticles, ultraporous films, electron-depleted.

Portable visible-blind photodetectors have a wide range of application including UV dosage monitoring for skin cancer prevention, flame and missile launch detection, optical communication and astronomy.[1-3] Si-based photodetectors, relying on n-p type semiconductor homojunction technology, are the most established commercial solution for measurement of ultraviolet light. These devices have some significant shortcomings including high operation voltage, the requirement of longpass filters to block low energy photons and cooling systems to reduce noise and leakage current. This significantly hinders their integration in wearable technologies and alternative solutions are intensively sought.[4, 5] Wide bandgap nanostructured semiconductors such as TiO_2 and ZnO are inherently visible-blind and can detect low concentration of ultraviolet light by a different mechanism, namely photo-generated variations in the concentration of surface-states.[2, 6]

Amongst highly performing materials, zinc oxide is a promising transparent metal oxide with a room temperature bandgap of 3.37 eV that matches well the lower edge of the visible light spectrum.[3, 7] Nano- and micro-structured ZnO photodetectors have been produced by several methods such as RF magnetron sputtering,[8] sol-gel,[9, 10] chemical vapor deposition[11] and

pulsed laser deposition[12] demonstrating significant improvement over bulk equivalents. Recently, Y.Ji et al.[13] have demonstrated fabrication of flexible devices with up to 1.56×10^3 photo- (I_{UV}) to dark-current (I_{dark}) ratio at a bias of 3 V by epitaxial growth of ZnO films on poly-ethylene-terephthalate (PET). Drop-coating of PET substrates with ZnO quantum dots - graphene solutions resulted in up to nearly 10 times higher I_{UV}/I_{dark} ratio indicating further optimization potential of morphology and composition. However, these results[14] were obtained at very high light intensities of 300[13] and 6 W.cm^{-2},[14] respectively, that are outside the range of many applications. To date, amongst the highest response to moderate UV light intensities has been achieved by electrospun ZnO-SnO$_2$ nanofibers films featuring a I_{UV}/I_{dark} of 4.6×10^3 at 10 V under a UV light intensity of 0.45 mW cm^{-2}.[5] Despite these significant improvements in the photo- to dark-current ratio, the magnitude of these devices' photo-current reached a maximum of only 35 nA at a bias of 2.4 V[1]. This is quite low and makes them incompatible with integrated CMOS micro-circuitry utilized in state-of-the-art portable devices such as smartphones, watches and security devices. Up to 900 µA photo-currents (Table 1)[15] have recently been achieved by more conductive but less light-sensitive structures. However, this results in high dark-currents of 1.5 µA and reduced signal to noise ratio[15] that undermine many of the high photo-current advantages.

Here, we present a novel hierarchical morphology for UV-blind photodetectors that results in excellent selectivity, record high milliampere photo-currents to very low ultraviolet light intensities and nanoampere dark-currents. We demonstrate the rapid ($\leq$ 100s) one-step synthesis and self-assembly of transparent ultraporous films composed of electron-depleted crystalline ZnO nanoparticles on low-cost glass substrates. Optimization of the film structure is performed resulting into absorption of more than 80% of the incoming ultraviolet radiation and transmission

of nearly 90% of the visible light. Characterization of the photodetector performance is pursued at very low light intensity (0.1 mW.cm^{-2}) resulting in the highest (3.4×10^5) photo- to dark-current ratio so far reported. These findings demonstrate a highly performing structure and a flexible and scalable platform technology for the rapid low-cost fabrication and integration of ultraviolet photodetectors in CMOS-compatible portable devices.

Figure 1a-c shows a schematic of the photodetector fabrication by liquid-fed spray flame synthesis and aerosol deposition. A hot ZnO nanoparticle aerosol was generated by atomization and combustion of a zinc naphtenate solution. The particle size was controlled by the Zn-atom precursor solution concentration that was set to 0.3 mol.l^{-1}. Transmission electron microscopy (TEM) analysis revealed (Figure 1d, inset) a spherical shape and a visible (d_{TEM}) average particle diameter of ca. 19 nm. Some rod-like structures were also observed (**Figure S1**). This in line with previous reports on the flame synthesis of larger ZnO nano-powders and it is attributed to preferential growth along the (100) plane.[16] This nanoparticle aerosol was orthogonally impinged on the water-cooled glass substrates resulting in the rapid self-assembly of ultraporous nanoparticle films with a very high film growth rate of 5.5 μm.min^{-1}. The substrate surface temperature (Figure 1c) was kept below 150 ℃ by a water-cooled substrate holder, and thus the temperature was too low to induce sintering of the ZnO nanoparticles within the maximal deposition time of 100 s utilized here. In fact, the particle diameters determined by nitrogen adsorption (BET) and TEM analysis of the powders collected from the substrate and filter were (d_{BET}) 16 nm and 18 nm and (d_{TEM}) 19 nm and 21 nm, respectively, confirming that no sintering finds place on the substrate during deposition. As a result, the film morphology (Figure 1d, inset and **Figure 2**b) was mainly determined by the particle deposition dynamics[17] resulting in an 98% porous network of nanoparticles that is hold together by weak van der Waals forces[18].

3

To decrease grain boundary barriers to electron conduction and increase the film mechanical stability, these fragile nanoparticle networks were post-sintered at 300 ºC for 12 h. This step had no measurable effects on the film morphology and crystallinity. It was, however, detectable by a small increase in crystal size (d_{XRD}) from 11.7 to 13.3 nm indicating inter-particle sintering and grain boundary necking (**Figure S2**). Figure 1e shows X-Ray Diffraction (XRD) and Fourier Transfer Infrared Spectroscopy (FTIR) patterns of particles collected from the filter and the photodetector substrates before and after sintering. All the XRD spectra correspond to the hexagonal wurtzite ZnO (JCPDS No. 36-1451) structure.[5, 19] Zinc oxide has a hexagonal-close-packed crystal structure composed of alternating planes of Zn and O atoms.[11] Height et al.[16] reported an increased XRD lattice aspect ratio between the (100) and (002) planes by increasing the concentration of dopants during flame-synthesis. This ultimately led to increasingly more accentuated rode-shaped nanostructures. Here, the (100)/(002) planes aspect ratio was found to be close to unity (1.05+/-0.05) and consistent for the particles collected from filter and substrate. This is in line with the predominant spherical-shape observed by TEM analysis (Figure S1) indicating homogenous particle growth by condensation and Brownian coagulation.

During and after fabrication, the photosensitive semiconductor surface can be contaminated by impurities. These usually undermine the device performance. The defect and impurity content in the flame-made ZnO nanoparticles and in the self-assembled ZnO films were characterized by FTIR (Figure 1e). The broad peaks at 3455 and 1146 cm^{-1} are assigned to the O-H stretching vibration of hydroxyl groups and attributed to adsorption of atmospheric moisture.[20] The residual hydroxyl peaks may be ascribed to the surface adsorption of ambient water. Two sharp peaks around 1600 and 1400 cm^{-1} are attributed to the asymmetrical and symmetrical stretching of zinc carboxylate, respectively.[21] The spectral signature of these C-H impurities completely

4

disappears upon sintering at 300 °C. As a result, the post-sintered ZnO films had a highly pure surface with no detectable organic or inorganic contaminants.

Figure 2a shows the optical transmittance of the ZnO films deposited on blank glass substrates as a function of the deposition time. All films were highly transparent to visible light with a relatively sharp cut-off below 370 nm. This is quite close to the end of the visible spectrum 400 nm and well within the UV-A range (400 - 320 nm). The film average integral transmittance for visible light was computed by subtraction of the fraction lost through the glass substrates (Figure 2a, circles) that decreased from 99% to 90% with increasing deposition time from 15 to 100 s in line with the increase film thickness. Optical images of the films placed over a printed paper (Figure 2a, inset) reveal a highly transparent surface up to a deposition time of 100 s.

This is particularly noteworthy as the resulting visible film thickness, measured by scanning electron microscopy (SEM), was ca. 10 μm (Figure 2d). This superior transparency was attributed to the unique film morphology and the non-scattering nature of the small ZnO primary particles. Figure 2b-c show exemplary films obtained by deposition of the hot nanoparticle aerosols on blank glass substrates for 100 s. At high magnification (Figure 2c), it is revealed that these aerosol self-assembled films have a very homogenous surface characterized by micro-sized pores between thin bridges of partially sintered ZnO nanoparticles resulting in an ultra-high average film porosity of 98%. Analysis of the film cross-sections (Figure 2d-e) revealed a homogeneous thickness over several hundred micrometres (Figure 2d) with no visible cracks and other defects.[22] This morphology is similar to that previously reported for as-prepared flame-made SnO_2 chemical sensors[18] further confirming that, independent of the composition, aerosol self-assembly leads to highly reproducible, statically equivalent film morphologies[17, 23].

However, in contrast to previous studies on aerosol-deposited SnO_2 and WO_3 films where high-temperature in-situ flame-annealing was utilized as a second step to mechanically stabilize the films and improve the electrical conductivity,[18, 24, 25] here the lower thermodynamic stability of ZnO enabled low temperature sintering, and thus to preserve the initial film porosity.

The photo- to dark-current (I_{UV}/I_{dark}) and the UV to visible light current (I_{UV}/I_{vis}) ratios are two key figures of merit for visible-blind photodetectors. **Figure 3**a shows the I-V response of the thickest films, with a deposition time of 100 s, to the edge of the visible spectrum (390 - 410 nm) and to representative UV-A radiation (350 - 370 nm). All the samples had very low dark-currents ($\leq$ 5 nA) up to a bias of 5 V corresponding to a total film resistance of nearly 1 Gohm at room temperature. This is attributed to the strong impact of surface states on the ZnO conductivity. For sufficiently small nanoparticles the high density of surface states results in significant electron depletion and thus very low dark current that represent an off-state of the device. In contrast under illumination (on-state), the I-V response was linear indicating an ohmic behaviour and sufficient availability of charge carriers to maintain a very high photo-current. At a wavelength of 370 nm and at a very low illumination intensity of 40 μW/cm^2, the photo-current reached up to 521 μA. This is more than five order of magnitude higher than the dark-current (3.61 nA) and demonstrate a highly sensitive sensing mechanism (**Figure S3**). It is important to note that although the light intensity used here (40 μW.cm^{-2}) was ca. 23-times lower than that commonly utilized to probe state-of-the-art metal-oxide photodetectors,[4] it still resulted in the highest I_{UV}/I_{dark} ratios (1.4×10^5) so far reported at low bias for wide bandgap semiconductor devices (Table 1).

This strong response is attributed to the unique morphology and composition of these films. With respect to the former, the quasi-non-scattering behaviour of these ultraporous hierarchical

structures maximizes the penetration of light down to the lowest nanoparticle layers (Figure 4a,c). This ensures the participation of the whole film in the sensing mechanism avoiding formation of light-insensitive domains that could act as bottlenecks reducing the increase in the film electrical conductivity and thus tampering the photo-current. This feature arises mainly from the high film porosity (98%). In stark contrast, deposition of the same nanoparticles by spin-coating method led to non-transparent, considerably less porous structures (40 - 60%). Figure S4 shows the transmittance spectra of an aerosol-deposited ultraporous film (red circles) and a spin-coated one (blue circles) composed of the same flame-made ZnO nanoparticles and having the same UV light (≤ 370 nm) transmittance. While in the visible domain, the ultraporous film (Figure S4, red circles) transmitted up to more than 90% of the incoming light, the denser one (blue circles) obtained by spin-coating (ca. 50% porosity) resulted in a low transmittance of ca. 20%. These results show that for the same nanomaterial composition ultraporous morphologies can drastically decrease light scattering. This is a key film structural property that enables synthesis of thick films with both high UV light absorption and penetration (Figure 4).

The other critical feature of these flame-made photodetectors is the ultra-fine ZnO nanoparticle size. Similarly to chemoresistive gas sensors,[22, 24] the ultraviolet light sensing mechanism of wide bandgap semiconductor depends from the ratio between their Debye length and the primary particle size[24] (**Figure 4e**). Due to the high porosity and hierarchical micro-pore size of these films, oxygen molecules can adsorb down to the deepest film layers (Figure 4a). Adsorption of O_2 on the ZnO nanoparticle surface results in the trapping of electron from the semiconductor conduction band.[24] This forms an electron-depleted layer within the semiconductor Debye length from the surface. During illumination, the photo-generated holes can travel to the surface along potential gradient and desorb oxygen molecules from the surface

7

(Figure 4c), resulting in an increase in the free carrier concentration within this depletion layer.[19] The transduction of this photo-response on the semiconductor conductivity, and thus photo-current, depends mainly from the ratio between the Debye length (δ) and the primary particle size (d_p). If d_p is larger than twice δ than a light-insensitive conduction channel is formed. This leads to relatively high dark current and exposure to UV light results only in the modulation of the conduction channel width. Decreasing this channel and thus the particle size increases the contribution of the light-sensitive domains to the total film conductivity resulting in higher photo-response. Usually, a main distinction is made for $d_p \gg 2\delta$ where the sensing mechanism is controlled by electron-transport at the grain boundary and $d_p > 2\delta$ where a significant portion of the bulk participate to light sensing (Figure 4e). In contrast, if $d_p \leq 2\delta$ than the whole particle is electron-depleted. This leads to highly resistive films with very low dark-currents. For this ultra-fine structures, exposure to ultraviolet light create a conduction channel resulting in a drastic increase in electrical conductivity and, potentially, very high photo-currents.

For our ZnO films the Debye length[22] can be computed as following[26]:

$$\delta = (\varepsilon\, kT/q^2 nc)^{1/2} \tag{1}$$

where ε is the static dielectric constant ($13.5 \times 8.5 \times 10^{-12}$ F/m in ZnO), k is the Boltzmann's constant (1.38×10^{-23} J/K), T is an absolute temperature (K), q is the electrical charge of the carrier (1.6×10^{-19} C), and nc is the carrier concentration (ca. 5×10^{16} cm^{-3})[27]. At room temperature ($T =$ 298 K) for ZnO, this results in a Debye length of ca. 19 nm. Considering that the primary particle size (d_{BET}) of the flame-made ZnO is 16 nm and the crystal size is 13 nm, here, the low dark-current and the very high photo- to dark-current ratio of these films are partially attributed to the fully electron-depleted state of the nanoparticle network (Figure 4e, $d_p \leq 2\delta$). This was confirmed by measurement of the resistance of the thick ZnO films aerosol-deposited for 100 s on gold

interdigitated electrodes with back heaters (Figure 3c). In pure nitrogen gas, the resistance decreased from 0.298 to 0.126 Mohm by increasing the sensor temperature from 150 to 240 ºC. This is line with the behaviour expected by for n-type semiconductors such as ZnO. Increasing the O_2 concentration from zero to 1% increased the film resistance by nearly 300 times (from 0.298 to 87 Mohm at 150 ºC). Similar results were obtained up to a film temperature of 240 ºC. This indicates that the conductivity of these ultraporous electron-depleted ZnO films is manly controlled by adsorption and desorption O_2 molecules. The quasi-non-scattering attribute of these ultraporous films is beneficial to ensure photo-excitation of these electron-depleted ZnO particles in the whole film structure and in particular in the lowest layers adjacent to the electrodes (Figure 4a,c).

To assess the impact of the film morphology on the resulting photodetector performance, the photo-response of denser (spin-coated) films having an average porosity of ca. 50% and the same UV optical density (0.7) of the ultraporous films (Figure S5) was further investigated. All dense films had a very high dark-current ranging from micro- to milliampere and very low photo- to dark-current ratio (ca. 1). The high dark-current was attributed (Figure 4b) to the denser morphology (ca. 50% porosity) of the spin-coated films that, for the same UV optical density (ca. 0.7), results in drastically higher film electrical conductivity than the ultraporous films. The relatively low photo-currents are attributed to the poor penetration of light in these dense morphologies (Figure 4d) that for optically dense, thick films does not allow photo-excitation of the bottom layers located near the electrodes. It should be noted that highly performing dense films of electron-depleted ZnO nanoparticles have been previously obtained by spin-coating.[2] However, these thin films had low UV optical density (ca. 0.3) and a very low electrode aspect ratio (ca. 0.75) resulting in lower photo-currents (ca. 1.8 µA at a bias of 5 V and 0.84 mW.cm^{-2}

9

UV light intensity) than the one achieved here by the ultraporous films (1.2 mA at 5 V and 0.1 mW.cm^{-2}). These results show that electron-depleted particles are critical but not sufficient to obtain milliampere high photo- and nanoampere low dark-currents at low UV light intensities. The ultraporous film morphology, developed here, is a key structural property required to individually optimize light absorption and electrical conductivity.

Figure 3b shows the spectral responsivity of the photodetectors as a function of the illumination wavelength and applied bias. It was observed that decreasing the wavelength below 400 nm sharply increased the responsivity that reached its peak value at about 370 nm. The responsivity increased by a factor of 7 (from 1.7 to 12.1 µA) by decreasing the wavelength from 390 to 370 nm. The sharp cut-off at wavelength of 370 nm is in good-agreement with the ZnO band gap of 3.37 eV ($\lambda = 368$ nm), confirming that these flame-made ZnO photodetectors are inherently visible-blind.

The photodetector responsivity was further investigated as a function of applied bias at different wavelengths in the UV-A and visible spectrum. A linear relationship (Figure 3d) was obtained with increasing bias from 0 to 5 V indicating no carrier mobility saturation or sweep effect up to the maximum applied bias. The ultraviolet selectivity, defined as a ratio of device response at a wavelength of 370 nm and 400 nm (Figure 3d, inset) reached 60 at a bias of 5 V. This is more than sufficient to enable very selective detection of low intensity of UV light without the need for high wavelength filters and further amplification.

Figure 3e shows the time response of an ultraporous ZnO nanoparticle film to UV light pulses ($\lambda = 370$ nm) with increasing intensity from 20 to 100 µW.cm^{-2}. The photo-current increased linearly by a factor of 4.5 (from 260 µA to 1.2 mA) with increasing light intensity from 20 to 100 µW.cm^{-2} resulting in a maximal I_{UV}/I_{dark} ratio of 3.4×10^5. This shows that in these

ultraporous electro-depleted nanoparticle films, the charge carrier photo-generation efficiency is proportional to the applied photon flux. The photo- to dark-current ratio obtained here at 100 $\mu W.cm^{-2}$ (3.4×10^5) is very high even in comparison to other highly performing photodetectors made of electron-depleted ZnO nanoparticles[2] that reached similar ratios (ca. 3×10^5) at higher light intensities (830 $\mu W.cm^{-2}$). Furthermore, to the best of our knowledge, achievement of milliampere photo-currents at low ultraviolet light intensity of 100 μWcm^2 while maintaining nanoampere dark-currents has not been previously reported (Table 1). This is a key improvement over state-of-the-art structures as it enables the direct integration of UV-photodetectors in CMOS-compatible micro-circuitry currently implemented in many wearable devices.

Figure 3f shows time-resolved photo-current measurements to alternating exposure to increasing UV light intensities (370 nm) and darkness. Regardless of the light intensities, the photo-current initially rapidly raised and thereafter gradually saturated under illumination, and then sharply dropped as the illumination was switched off. The initial response time of the ultraporous ZnO films was less than 0.3 s in line with previous reports on electron-depleted ZnO nanoparticles[2]. Rise and decay times were computed from the time required for the current to increase to 90% of the steady-state photo-current value and to decrease again by 90%, respectively. The rise and decay times during the on/off cycles were 250 and 150 s, respectively, and thus in line with that expected for pure ZnO nanostructured photodetectors (Table 1). The relatively long times required to reach a steady-state photo- and dark-current are attributed to the chemi/physisorption and photo-desorption of oxygen molecules from the ZnO nanoparticle surface (Figure 4).[15, 28] The rise and decay time could be further improved by replacing the ZnO nanoparticles with recently reported materials such as ZnS[4, 29] that offer faster photo-current dynamics.

In conclusion, we have developed a novel structural design for CMOS-compatible visible-blind photodetectors featuring ultra-high milliampere photo-currents, very low dark currents, very low UV intensity detection limit and low operation voltages. This excellent performance was attributed to the quasi-non-scattering optical properties and electron-depleted composition of these ultraporous nanoparticle films. Decreasing the primary particle size below twice the ZnO Debye length and providing ultraporous film morphology enhanced light penetration and adsorption/desorption of oxygen molecules from the nanoparticle surface resulting in an on/off switch behaviour to UV light exposure. Furthermore, we have demonstrated a flexible and low-cost platform technology for the rapid fabrication and integration of ultraporous electron-depleted nanoparticle photodetectors in micro-machinable circuitry. This concept can be applied to other highly performing semiconductors such as wide bandgap SnO_2 for selective UV-B detection and fast-responding ZnS[4, 29] for fiber optics.

Experimental

A flame spray pyrolysis (FSP) system was used for the synthesis and direct deposition of ZnO nanoparticles films onto the glass substrates featuring a set of interdigitated electrodes. A solution of Zinc Naphthenate (10% Zn, Sigma Aldrich) and Xylene (Sigma Aldrich) was prepared with a total Zn-metal atom concentration of 0.3 mol.l^{-1}. This solution was supplied at a rate of 5 ml.min^{-1} through a syringe pump, and dispersed into a fine spray with 7 L.min^{-1} oxygen at a constant pressure drop of 2 bars. The spray was ignited by supporting premixed methane/oxygen flames (CH_4 = 1.2 L.min^{-1}, O_2 = 2 L.min^{-1}). A water-cooled substrate holder placed at 20 cm height above the burner (HAB) was utilized to keep the substrate temperature below 150 °C. The photodetector substrates were made of glass with interdigitated gold lines with 5µm width and spacing and a total electrode area of 7×5 mm (G-IDEAU5, DropSens,

Oviedo, Spain). More details about the device design and geometry are included in the Supplementary Information, Figure S6. All substrates were cleaned with multiple ethanol/drying cycles before nanoparticles deposition. For measurement of the film resistance in pure nitrogen gas and with 1% oxygen, alumina substrate (0.8 mm thick) with interdigitated Pt lines with 200 μm width and 300 μm spacing were used. The substrates had a Pt resistance temperature detector (RTD) on one side and a Pt heater on the other side. The overall dimensions of the alumina substrate were 15 mm × 13 mm (Electronic Design Center, Case Western Reserve University, Cleveland, OH, USA).

The morphology and patterning characteristics of the deposited particles and films were investigated by a Hitachi H7100FA transmission electron microscope (TEM) at 100 kV and an analytical scanning electron microscopy (SEM), using Zeiss Ultraplus (FESEM) at 3 kV. The crystal phases, size (d_{XRD}) and surface compositions were characterized by X-Ray diffraction using Bruker system (XRD, D_2 Phaser, U.S.A) equipped with Cu Ka radiation of average wavelength 1.54059 Å. The Brunauer-Emmett-Teller specific surface area (BET, SSA) of the deposited nanoparticles was measured by N_2 adsorption using a porosity analyzer (Micromeritics, TriStar II, U.S.A). The nanoparticles were degassed at 200 °C for 8 hours prior to analysis. The substrates were kept in a furnace (Brother High Temperature Furnace XD-1.2KN) at 300 °C for 12 h at ambient pressure prior photo-detecting tests, to stabilize the nanoparticle size and avoid resistive-sintering during the photo-detection measurements.

The optical properties of ZnO thin films deposited by FSP were carried out using the TECAN infinite spectrophotometer (200 PRO) and all measurements were carried out at room temperature. For I-V measurements, DC currents were measured using a Picoammeter / Voltage source (Model 6487, Keithley). The detection of UV light was performed using a Newport

Xenon lamp source 66920 and the UV-vis absorption spectra were recorded in the wavelength range 250–500 nm using Princeton Instrument Acton SP2500 (0.500m Imaging Triple Grating Monochromator/Spectrograph).

Supporting Information

Supporting Information is available from the Wiley Online Library or from the author (TEM and SEM analysis of particles and film morphology, Additional I-V characterization results).

Acknowledgements

References

[1]   D. Gedamu, I. Paulowicz, S. Kaps, O. Lupan, S. Wille, G. Haidarschin, Y. K. Mishra, R. Adelung, *Adv. Mater.* **2014**, 26, 1541.
[2]   Y. Jin, J. Wang, B. Sun, J. C. Blakesley, N. C. Greenham, *Nano Lett.* **2008**, 8, 1649.
[3]   J. Sun, F.-J. Liu, H.-Q. Huang, J.-W. Zhao, Z.-F. Hu, X.-Q. Zhang, Y.-S. Wang, *Appl. Surf. Sci.* **2010**, 257, 921.
[4]   L. Hu, J. Yan, M. Liao, H. Xiang, X. Gong, L. Zhang, X. Fang, *Adv. Mater.* **2012**, 24, 2305.
[5]   W. Tian, T. Zhai, C. Zhang, S.-L. Li, X. Wang, F. Liu, D. Liu, X. Cai, K. Tsukagoshi, D. Golberg, Y. Bando, *Adv. Mater.* **2013**, 25, 4625.
[6]   N. Hongsith, E. Wongrat, T. Kerdcharoen, S. Choopun, *Sens. Actuators, B* **2010**, 144, 67.
[7]   S. M. Hatch, J. Briscoe, S. Dunn, *Adv. Mater.* **2013**, 25, 867.
[8]   R. Liu, D. Jiang, Q. Duan, L. Sun, C. Tian, Q. Liang, S. Gao, J. Qin, *Appl. Phys. Lett.* **2014**, 105.
[9]   S.-E. Ahn, H. J. Ji, K. Kim, G. T. Kim, C. H. Bae, S. M. Park, Y.-K. Kim, J. S. Ha, *Appl. Phys. Lett.* **2007**, 90.
[10] M. H. Mamat, Z. Khusaimi, M. Z. Musa, M. Z. Sahdan, M. Rusop, *Mater. Lett.* **2010**, 64, 1211.
[11] J. Liu, R. Lu, G. Xu, J. Wu, P. Thapa, D. Moore, *Adv. Funct. Mater.* **2013**, 23, 4941.

[12] N. Hernandez-Como, S. Moreno, I. Mejia, M. A. Quevedo-Lopez, *Semicond. Sci. Technol.* **2014**, 29, 085008.

[13] L. Ji, C. Wu, C. Lin, T. Meen, K. Lam, S. Peng, S. Young, C. Liu, *Jpn. J. Appl. Phys.* **2010**, 49, 052201.

[14] D. Ick Son, H. Yeon Yang, T. Whan Kim, W. Il Park, *Appl. Phys. Lett.* **2013**, 102, 021105.

[15] J. Cheng, Y. Zhang, R. Guo, *J. Cryst. Growth* **2008**, 310, 57.

[16] M. J. Height, L. Mädler, S. E. Pratsinis, F. Krumeich, *Chem. Mater.* **2005**, 18, 572.

[17] T. D. Elmøe, A. Tricoli, J.-D. Grunwaldt, S. E. Pratsinis, *J. Aerosol Sci.* **2009**, 40, 965.

[18] A. Tricoli, M. Graf, F. Mayer, S. Kuühne, A. Hierlemann, S. E. Pratsinis, *Adv. Mater.* **2008**, 20, 3005.

[19] W. Tian, C. Zhang, T. Zhai, S.-L. Li, X. Wang, J. Liu, X. Jie, D. Liu, M. Liao, Y. Koide, D. Golberg, Y. Bando, *Adv. Mater.* **2014**, 26, 3088.

[20] S. Muthukumaran, R. Gopalakrishnan, *Opt. Mater.* **2012**, 34, 1946.

[21] G. Xiong, U. Pal, J. G. Serrano, K. B. Ucer, R. T. Williams, *Phys. Stat. Sol. (c)* **2006**, 3, 3577.

[22] A. Tricoli, M. Righettoni, A. Teleki, *Angew. Chem. Int. Ed.* **2010**, 49, 7632.

[23] A. Tricoli, T. D. Elmøe, *AIChE J.* **2012**, 58, 3578.

[24] A. Tricoli, M. Graf, S. E. Pratsinis, *Adv. Funct. Mater.* **2008**, 18, 1969.

[25] M. Righettoni, A. Tricoli, S. E. Pratsinis, *Chem. Mater.* **2010**, 22, 3152.

[26] H. Ogawa, M. Nishikawa, A. Abe, *J. Appl. Phys.* **1982**, 53, 4448.

[27] M. S. White, D. C. Olson, S. E. Shaheen, N. Kopidakis, D. S. Ginley, *Appl. Phys. Lett.* **2006**, 89, 143517.

[28] O. Lupan, G. Chai, L. Chow, G. A. Emelchenko, H. Heinrich, V. V. Ursaki, A. N. Gruzintsev, I. M. Tiginyanu, A. N. Redkin, *Phys. Status Solidi A* **2010**, 207, 1735.

[29] A. Bera, D. Basak, *ACS Appl. Mater. Interfaces* **2010**, 2, 408.

[30] C. Soci, A. Zhang, B. Xiang, S. A. Dayeh, D. P. R. Aplin, J. Park, X. Y. Bao, Y. H. Lo, D. Wang, *Nano Lett.* **2007**, 7, 1003.

[31] A. Manekkathodi, M.-Y. Lu, C. W. Wang, L.-J. Chen, *Adv. Mater.* **2010**, 22, 4059.

[32] K. Liu, M. Sakurai, M. Liao, M. Aono, *J. Phys. Chem. C* **2010**, 114, 19835.

[33] Y. Hou, Z. Mei, X. Du, *J. Phys. D: Appl. Phys.* **2014**, 47, 283001.
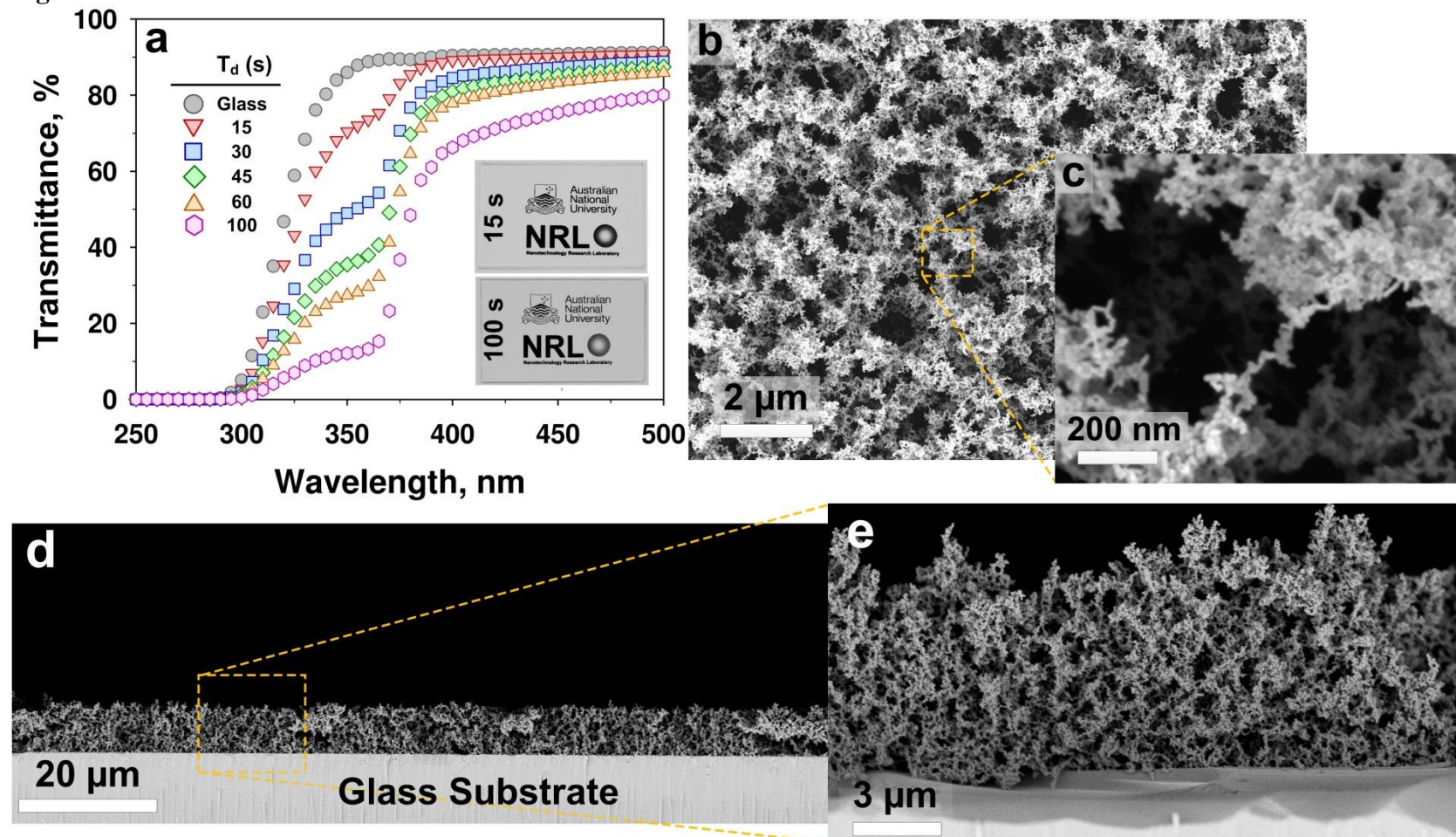
Figure 1
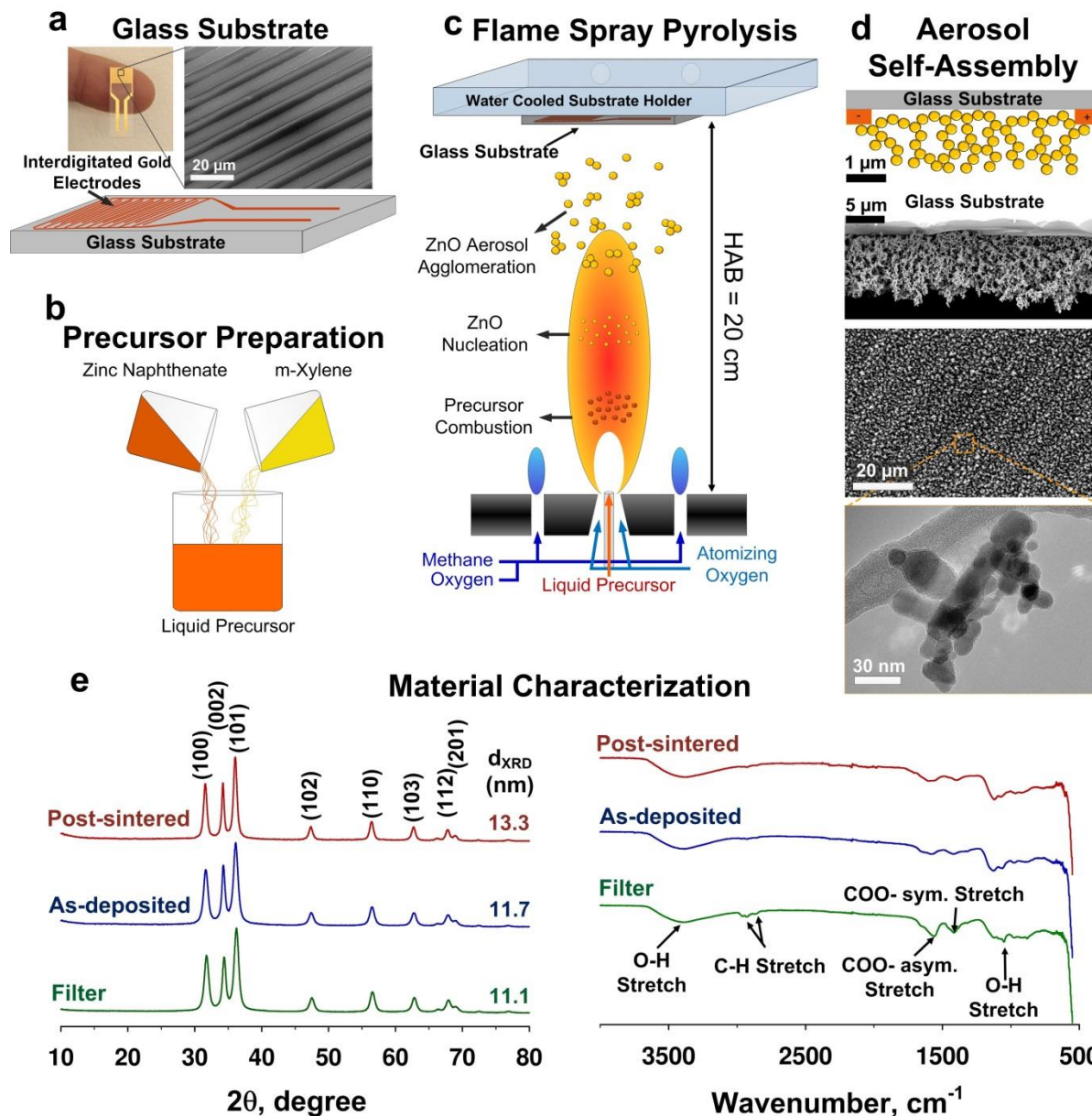
Figure 1. Schematics of a (a) photodetector substrate and (b,c) flame spray pyrolysis synthesis and aerosol self-assembly of (d) ultraporous films made of electron-depleted ZnO nanoparticles at 20 cm height above the burner (HAB). The resulting films are (d) uniform and homogenously composed of mostly spherical-particles with an average TEM size of 19 nm. The (e) XRD and FTIR patterns of the ZnO particles collected on the filters and substrate before and after sintering reveal a wurtzite crystal structure and high purity.

Figure 2

Figure 2. Optical transmittance spectra of ultraporous ZnO films deposited on blank glass substrates as a function of the aerosol deposition time and of a blank glass substrate (circles). a) Inset: Optical images of ZnO films deposited for 15 and 100 s on glass substrates placed over a printed paper. SEM images of an exemplary film deposited for 100 s on a glass substrate reveal a highly porous and uniform (b,c) top surface and (d,e) cross-section.

Figure 3
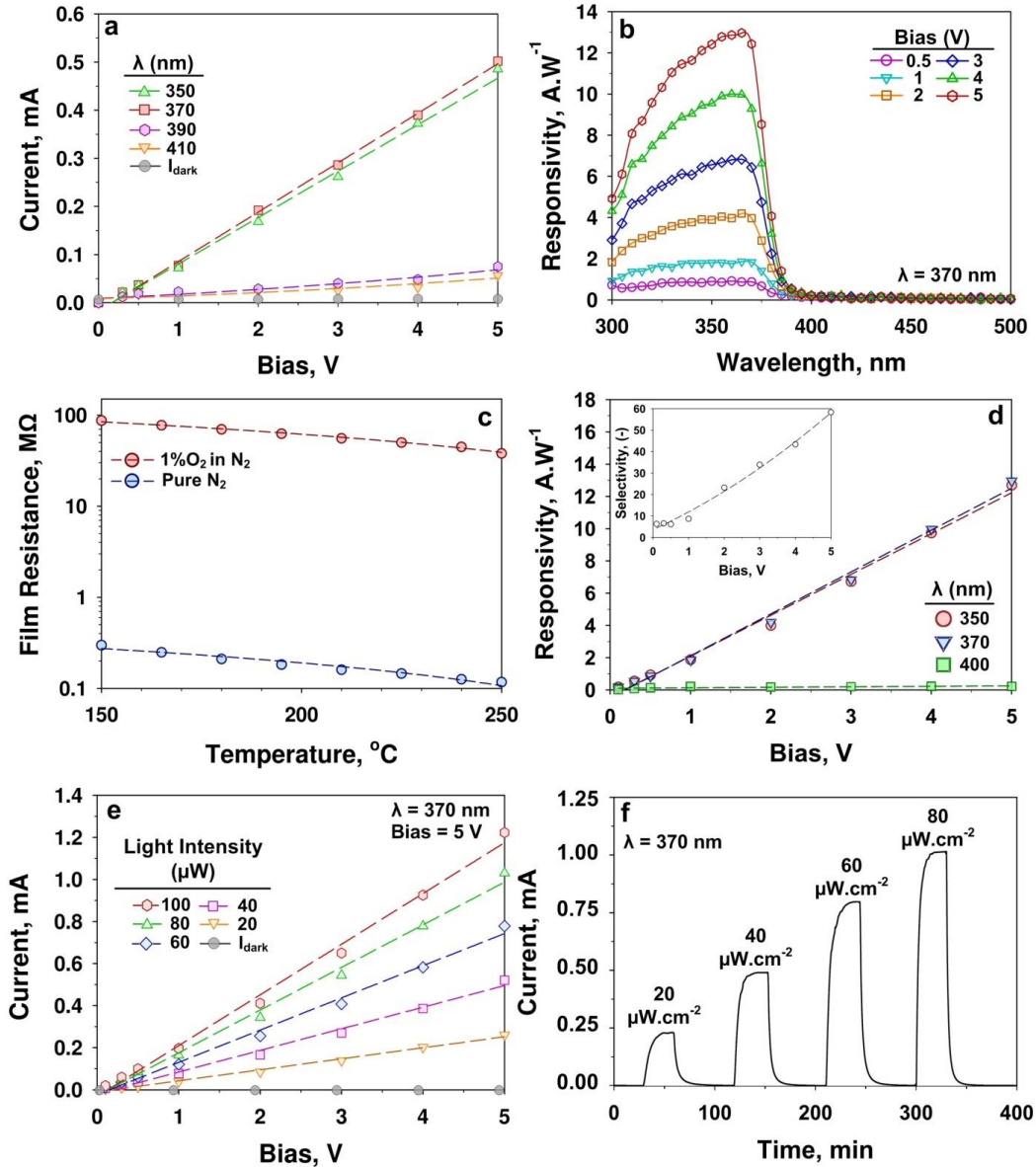
Figure 3. (a) I-V characteristics and (b) responsivity of the ZnO ultraporous photodetectors as a function of the applied light and bias. (c) Film resistance in N_2 as a function of the temperature O_2 content. (d) Photodetector responsivity and (inset) I_{370}/I_{400} UV-visible selectivity as function of applied bias at a wavelength of 350, 370 nm and 400 nm light illumination. (e) Photo-current as a function of applied bias and inset, light intensity demonstrating milliampere currents at low light intensities of 100 μW. (f) Time-dependent photodetector response to alternative exposure to increasing light intensity at a bias of 1 V and a wavelength of 370 nm.

Figure 4
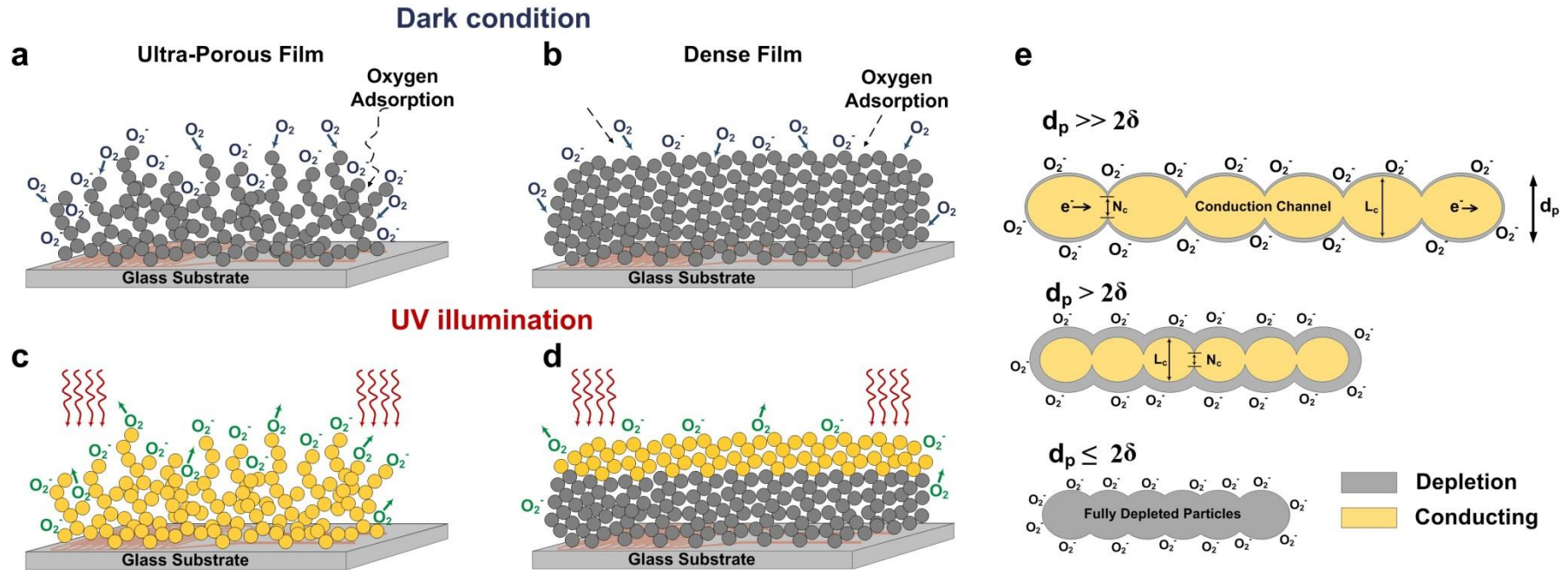
Figure 4. Schematic model of the photo-response mechanisms of ZnO nanoparticle films based on the adsorption and desorption of molecular oxygen[2] in (a,c) ultraporous and (b,d) dense films. As a function of the ratio between the particle diameter (d_p) and the Debye length (δ), three photo-detection mechanisms (e) are expected[6]. Particle size larger than twice the Debye length of ZnO leads to grain boundary or surface controlled responses with limited photo- to dark-current ratios, whereas particle size smaller than twice the Debye length leads to fully depleted nanostructures with an on/off switching behavior. The quasi-non-scattering properties of (a,c) these ultraporous electron-depleted nanoparticle films enable penetration of light to the lowest particle layers close to the electrodes. In contrast, the dense films (b,d) have significantly lower transmittance and may result in the formation of light-insensitive domains.

Table 1. Figures of merit of state-of-the-art wide bandgap ZnO photodetectors.

| Photodetector	d_p	Bias	Dark-Current	Photo-current	I_{photo}/I_{dark} Ratio	Intensity	Rise Time	Decay Time	Ref.
ZnO ultraporous nanoparticle networks	20 nm	5 V	3.61 nA	1.2 mA	3.4×10^5	100 μW/cm^2	~250 s	~150 s	This Work
				512 μA	1.4×10^5	40 μW/cm^2			
				260 μA	7.2×10^4	20 μW/cm^2			
ZnO nanotetrapods network	--	2.4 V	--	~ 35 nA	4.5×10^3	$\approx$20 mW.cm^{-2}	68 ms	32 ms	[1]
ZnO nanoneedles	50-200 nm	0.3 V	--	~ 250nA	312	$\approx$15 mW.cm^{-2}	22 s	7-12 s	[1]
Colloidal ZnO nanoparticles	10 nm	5 V	7 pA	1.8 μA	$\approx2.6\times10^5$	830 μW/cm^2	--	--	[2]
ZnS/ZnO nanobelts	~ 100 nm	5 V	0.67 μA	4.64 μA	6.92	0.91 mW.cm^{-2}	0.3 s	1.7 s	[4]
ZnO-SnO$_2$	100-150 nm	10 V	1.7 pA	7.9 nA	4.6×10^3	0.45 mW.cm^{-2}	32.2 s	7.8 s	[5]
ZnO nanowire	30 nm	5 V	15 pA	270 pA	18	--	43.7 s	--	[9]
ZnO epitaxial films	--	3 V	--	--	1.56×10^3	300 W.cm^{-2}	--	--	[13]
ZnO quantum dot/graphene	5 nm	3 V	91.6 pA	0.83 μA	1.1×10^4	6 W.cm^{-2}	2 s	1 s	[14]
ZnO microtubes	~ 100 nm	5 V	1.5 μA	900 μA	600	21.7 mW.cm^{-2}	5.9 s	638 s	[15]
ZnS-coated ZnO arrays	100 nm	3 V	--	--	1.25	150 W.cm^{-2}	120 s	180 s	[28]
ZnO nanowire	60-70 nm	5 V	10 nA	100 μA	10^4	40 mW.cm^{-2}	--	--	[30]
ZnO nanorods	150-300 nm	5 V	--	13 μA	85	--	> 500 s	500 s	[31]
ZnO nanowire	150 nm	1 V	0.13 pA	--	1000	1.3 mW.cm^{-2}	40 s	300 s	[32]
ZnO nanowire array	40 nm	5 V	~ 71 μA	~ 100 μA	1.4	--	0.4 ms	--	[33]

Table of Content
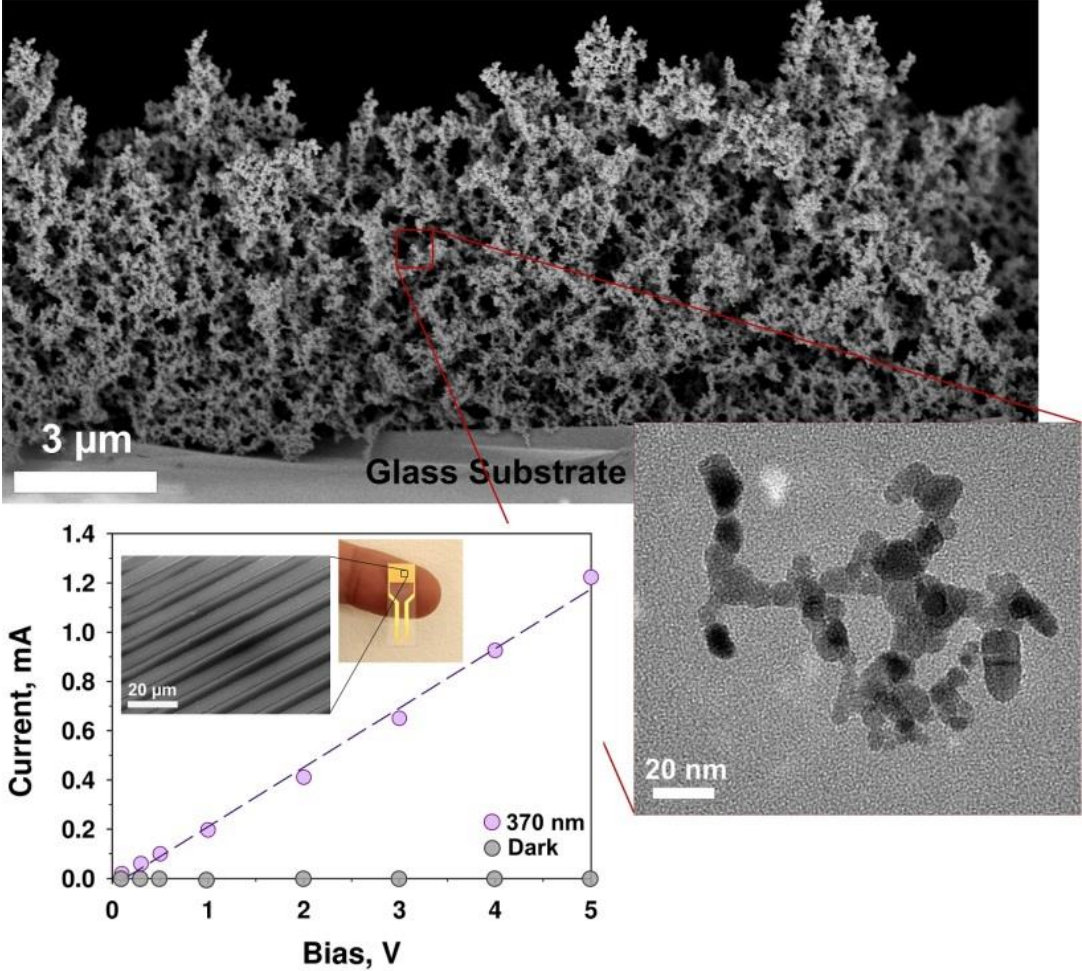
Figure S1
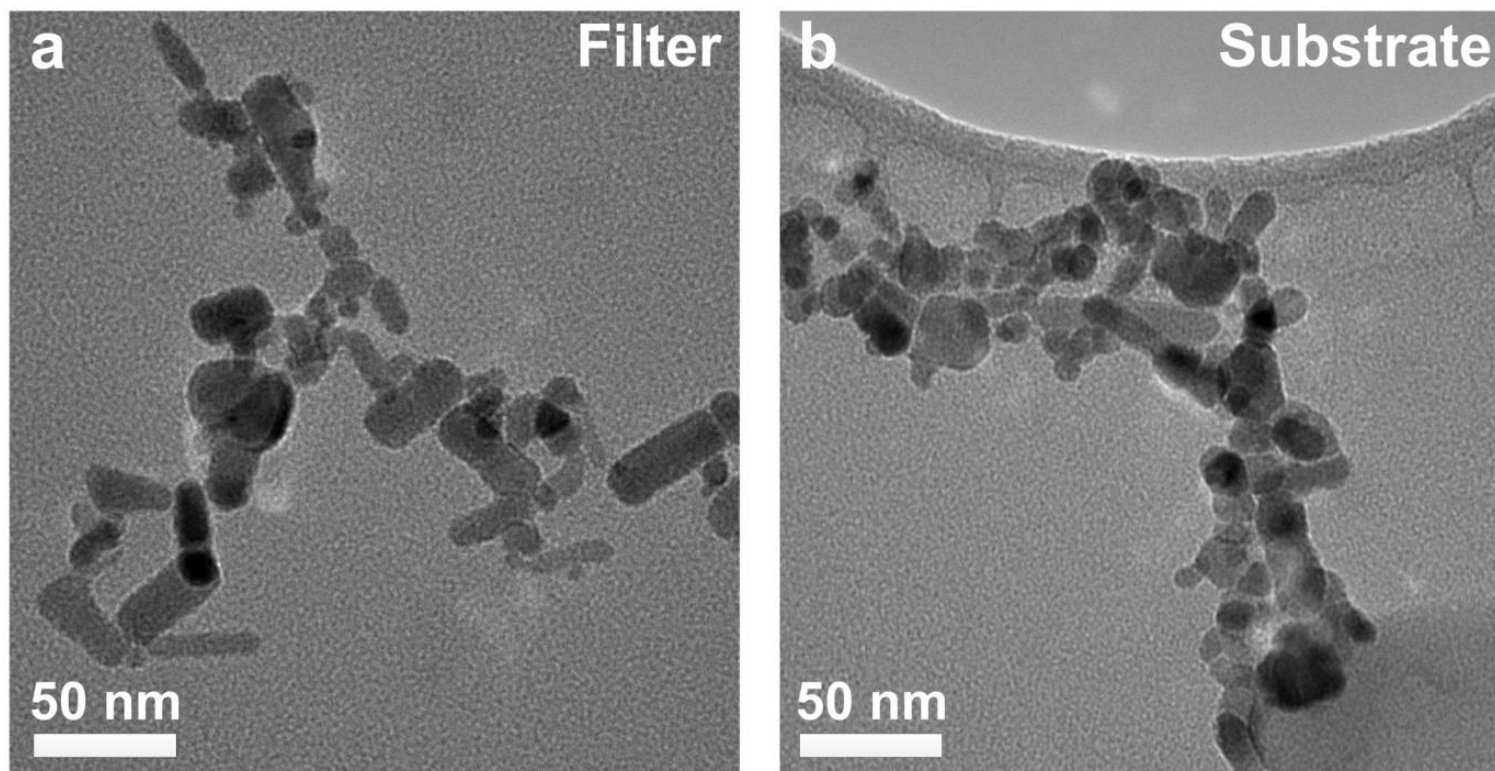
Figure S1. TEM images of flame-made ZnO particles collected from (a) the filter (HAB of 50 cm) and (b) the substrate (HAB of 20 cm).

Figure S2
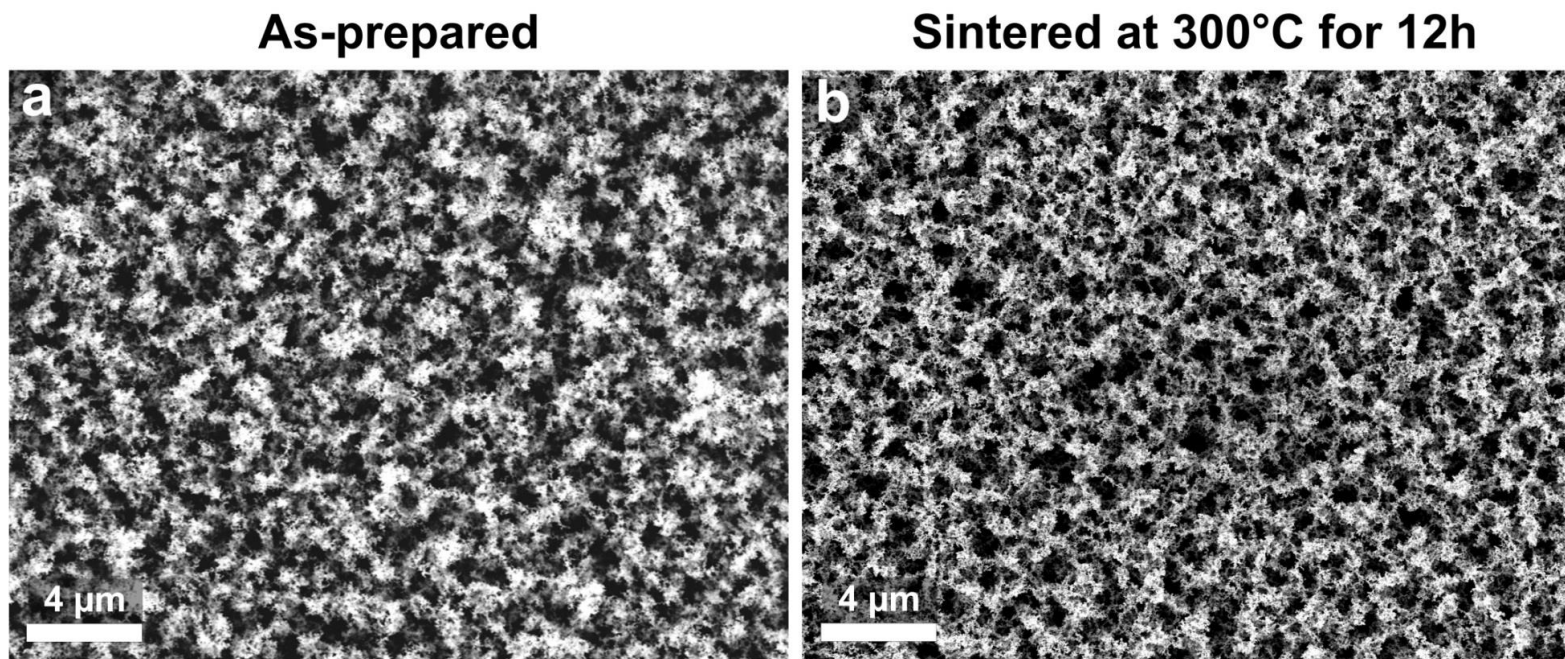
Figure S2. SEM images of the ZnO particles aerosol-deposited on glass substrates (a) before and (b) after sintering at 300 ℃ for 12h (HAB of 20 cm).
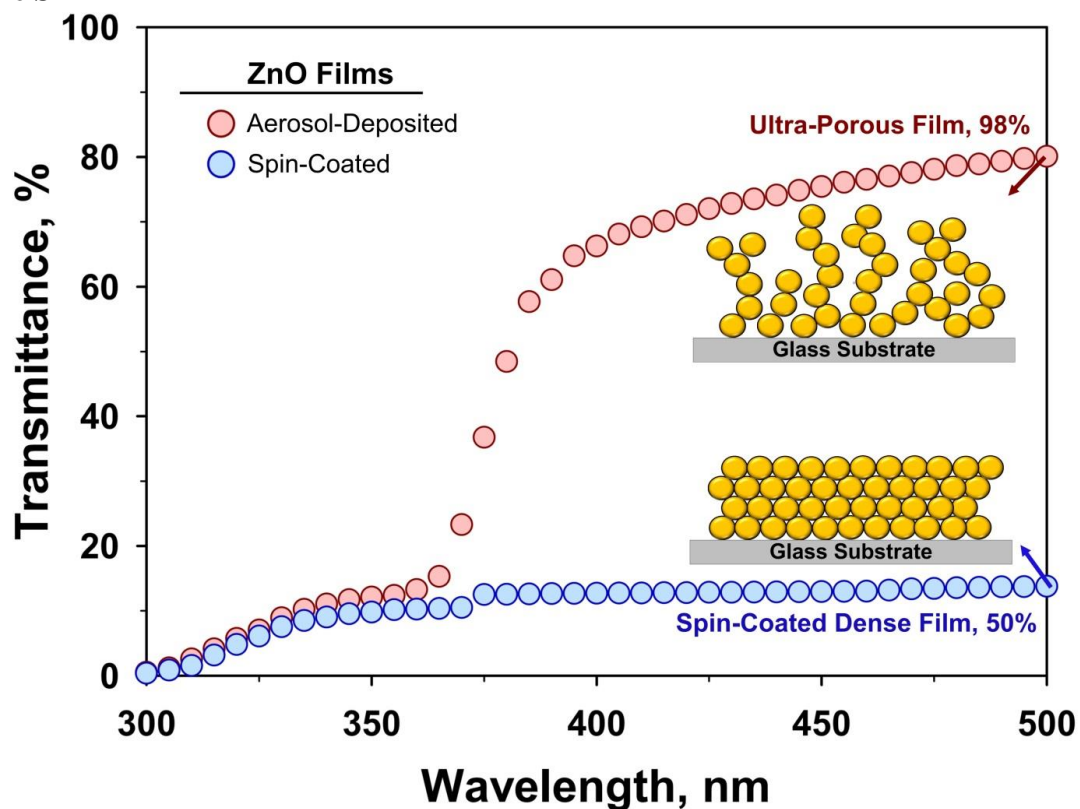
Figure S3
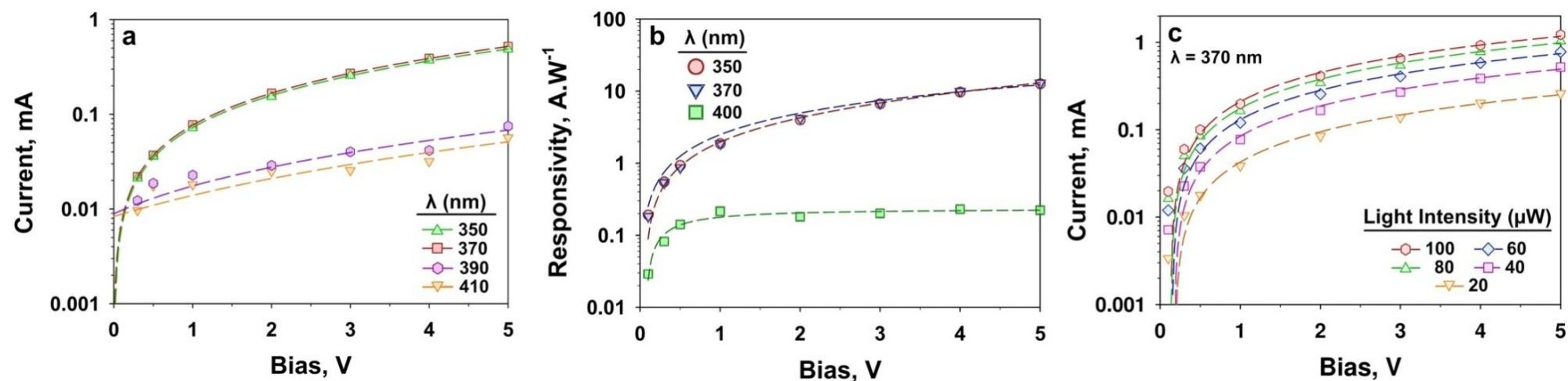
Figure S3. (a) I-V characteristics of ZnO ultraporous films at different light wavelengths and under dark condition as a function of applied bias. (b) The photodetector responsivity as function of applied bias under UV (350 and 370 nm) and visible (400 nm) light illumination. (c) Photo-current as a function of applied bias and light intensity.

Figure S4

Figure S4. Transmittance spectra of an aerosol-deposited ultraporous film (red circles) and a spin-coated one (blue tcircles) both composed of the same flame-made ZnO nanoparticles and having the same light transmittance at the edge of the ZnO bandgap (ca. 370 nm).
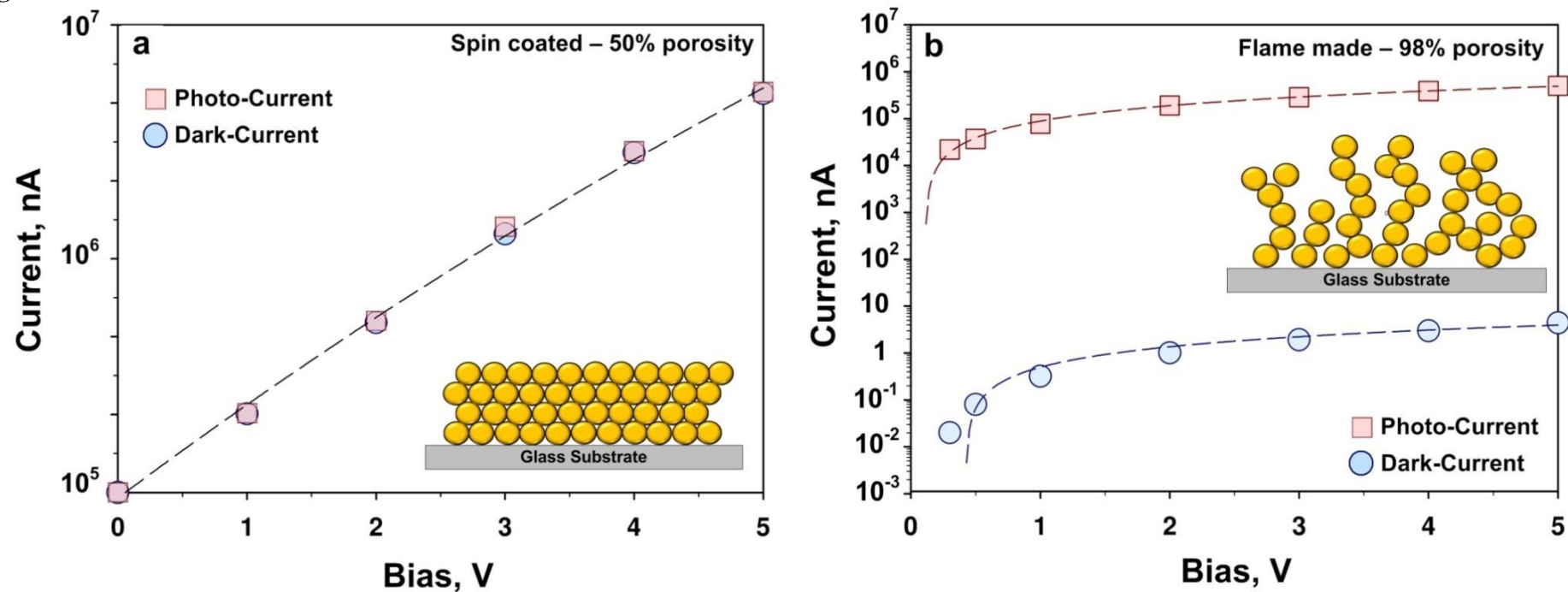
Figure S5

Figure S5. Photo- and dark-currents of (a) a spin-coated and (b) ultraporous films composed of the same flame-made ZnO nanoparticles and having both an optical density of ca. 0.7 at λ of 370 nm.
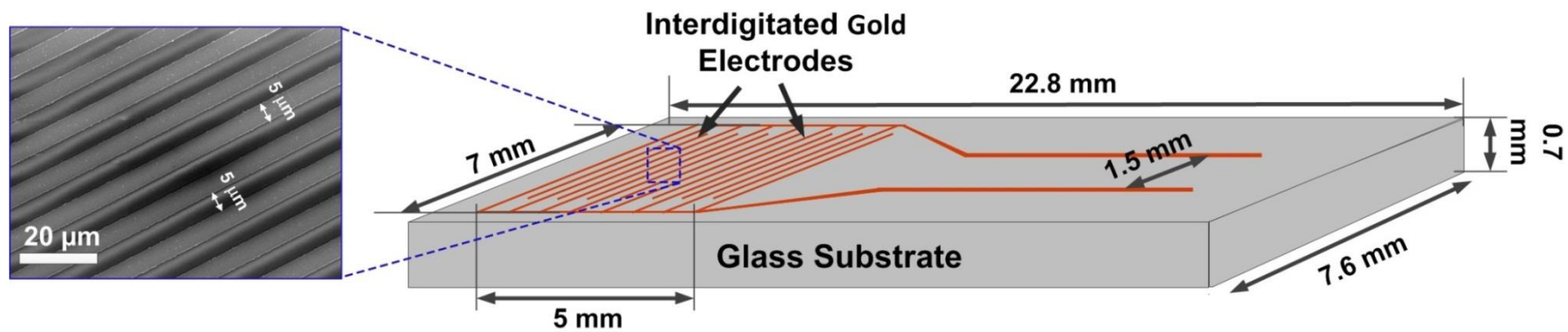
Device Design and Geometry

Figure S6. Schematic of the interdigitated gold electrode layout used as photodetector substrates.